THE ASTROPHYSICAL JOURNAL, 595:352–364, 2003 September 20

ONE-ARMED SPIRAL INSTABILITY IN DIFFERENTIALLY ROTATING STARS

MOTOYUKI SAIJO
Department of Physics, Kyoto University, Kyoto 606-8502, Japan;
saijo@tap.scphys.kyoto-u.ac.jp

THOMAS W. BAUMGARTE[1]
Department of Physics and Astronomy, Bowdoin College, 8800 College Station, Brunswick, ME 04011;
tbaumgar@bowdoin.edu

AND

STUART L. SHAPIRO[2,3]
Department of Physics, University of Illinois at Urbana-Champaign, 1110 West Green Street, Urbana, IL 61801;
shapiro@astro.physics.uiuc.edu
Received 2003 January 22; accepted 2003 June 4

ABSTRACT

We investigate the dynamical instability of the one-armed spiral $m = 1$ mode in differentially rotating stars by means of 3 + 1 hydrodynamical simulations in Newtonian gravitation. We find that both a soft equation of state and a high degree of differential rotation in the equilibrium star are necessary to excite a dynamical $m = 1$ mode as the dominant instability at small values of the ratio of rotational kinetic to gravitational potential energy, $T/|W|$. We find that this spiral mode propagates outward from its point of origin near the maximum density at the center to the surface over several central orbital periods. An unstable $m = 1$ mode triggers a secondary $m = 2$ bar mode of smaller amplitude, and the bar mode can excite gravitational waves. As the spiral mode propagates to the surface it weakens, simultaneously damping the emitted gravitational wave signal. This behavior is in contrast to waves triggered by a dynamical $m = 2$ bar instability, which persist for many rotation periods and decay only after a radiation reaction–damping timescale.

Subject headings: gravitation — hydrodynamics — instabilities — stars: neutron — stars: rotation

1. INTRODUCTION

Stars in nature are usually rotating and may be subject to nonaxisymmetric rotational instabilities. An exact treatment of these instabilities exists only for incompressible equilibrium fluids in Newtonian gravity (e.g., Chandrasekhar 1969; Tassoul 1978). For these configurations, global rotational instabilities may arise from nonradial toroidal modes $e^{im\varphi}$ (where $m = \pm 1, \pm 2, \ldots$ and φ is the azimuthal angle).

For sufficiently rapid rotation, the $m = 2$ bar mode becomes either *secularly* or *dynamically* unstable. The onset of instability can typically be identified with a critical value of the nondimensional parameter $\beta \equiv T/|W|$, where T is the rotational kinetic energy and W the gravitational potential energy. Uniformly rotating incompressible stars in Newtonian theory are secularly unstable to bar mode formation when $\beta \geq \beta_{\rm sec} \simeq 0.14$. This instability can grow only in the presence of some dissipative mechanism, such as viscosity or gravitational radiation, and the associated growth timescale is the dissipative timescale, which is usually much longer than the dynamical timescale of the system. By contrast, a dynamical instability to bar mode formation sets in when $\beta \geq \beta_{\rm dyn} \simeq 0.27$. This instability is independent of any dissipative mechanisms, and the growth time is the hydrodynamic timescale.

Determining the onset of the dynamical bar mode instability, as well as the subsequent evolution of an unstable star, requires a fully nonlinear hydrodynamic simulation. Simulations performed in Newtonian gravity (e.g., Tohline, Durisen, & McCollough 1986; Durisen et al. 1986; Williams & Tohline 1988; Houser, Centrella, & Smith 1994; Smith, Houser, & Centrella 1996; Houser & Centrella 1996; Pickett, Durisen, & Davis 1996; Toman et al. 1998; New, Centrella, & Tohline 2000) have shown that $\beta_{\rm dyn}$ depends only very weakly on the stiffness of the equation of state. Once a bar has developed, the formation of a two-arm spiral plays an important role in redistributing the angular momentum and forming a core-halo structure. Both $\beta_{\rm dyn}$ and $\beta_{\rm sec}$ are smaller for stars with a high degree of differential rotation (Tohline & Hachisu 1990; Pickett et al. 1996; Shibata, Karino, & Eriguchi 2002; Shibata, Karino, & Eriguchi 2003). Simulations in relativistic gravitation (Shibata, Baumgarte, & Shapiro 2000; Saijo et al. 2001) have shown that $\beta_{\rm dyn}$ decreases with the compaction of the star, indicating that relativistic gravitation enhances the bar mode instability. To efficiently use computational resources, most of these simulations have been performed under certain symmetry assumptions (e.g., π-symmetry) that do not affect the growth of the $m = 2$ bar mode but suppress any $m = 1$ modes.

Recently, Centrella et al. (2001) reported that such $m = 1$ "one-armed spiral" modes are dynamically unstable at surprisingly small values of $T/|W|$. Centrella et al. (2001) found this instability in evolutions of highly differentially rotating equilibrium polytropes with polytropic index $n = 3.33$. Typically, these equilibria have a "toroidal" structure, so that the maximum density is not located at the

[1] Department of Physics, University of Illinois at Urbana-Champaign, 1110 West Green Street, Urbana, IL 61801.
[2] Department of Astronomy, University of Illinois at Urbana-Champaign, 1002 West Green Street, Urbana, IL 61801.
[3] NCSA, University of Illinois at Urbana-Champaign, Urbana, IL 61801.

geometric center but rather on a toroid rotating about the center.

It is possible that the $m = 1$ instability in equilibrium stars is related to that arising in protostellar disk systems. This instability originally was found in nearly Keplerian thin gaseous disks around central point masses, both numerically (Adams, Ruden, & Shu 1989; Heemskerk, Papalozizou, & Savonije 1992) and analytically (Shu et al. 1990). The central point mass moves away from the center of mass of the whole system because of a perturbation and this displacement triggers the instability. This particular mode of instability occurs only when the mass ratio $M_{\rm disk}/M_{\rm total}$ exceeds 0.2. An $m = 1$ instability has also been found in thick self-gravitating protostellar tori (Woodward, Tohline, & Hachisu 1994) and protostellar disks (Laughlin & Bodenheimer 1994), as well as in finite fluid cores surrounded by disk halos (Pickett et al. 1996). In the latter case, the instability arises from the internal interaction between different regions of a single continuous body, and the disk does not need to satisfy the above mass criterion to trigger the $m = 1$ instability (see also Bonnell 1994 for an example of an unstable central accreting object surrounded by a rotationally supported gas disk).

The purpose of this paper is to study further the conditions under which a dynamical $m = 1$ instability is excited. We vary both the polytropic index, i.e., the stiffness of the equation of state, and the degree of differential rotation to isolate their effects on the instability. Since the onset of rotational instabilities is often characterized by β, we keep this value approximately fixed in our sequences. We find that a soft equation of state and a high degree of differential rotation are both necessary to dynamically excite the $m = 1$ mode at the small value of $\beta = 0.14$ chosen in this paper. We find that a toroidal structure is not sufficient to trigger the $m = 1$ instability, but our findings suggest that a toroidal structure may be necessary.

While our goal is to gain a deeper understanding of the nature of the $m = 1$ instability as opposed to simulating realistic astrophysical scenarios, we point out that there exist evolutionary sequences that may well lead to rapidly and highly differentially rotating configurations. For example, cooling by thermal emission from a rotating star will cause the star to contract and spin up. If internal viscosity and magnetic fields are sufficiently weak, this process will lead to differential rotation even if the initial configuration is rotating uniformly. This scenario may arise in supermassive stars, for which the equation of state is dominated by radiation pressure and may be modeled by a (soft) $n = 3$ polytrope. In the absence of viscosity and magnetic braking, the star will contract quasi-statically as it cools to a toroidal configuration, which may be subject to $m = 1$ or $m = 2$ instabilities (New & Shapiro 2001). Stellar collisions and mergers may also lead to differentially rotating stars. For the coalescence of binary neutron stars (Shibata & Uryū 2000, 2002), the presence of differential rotation may temporarily stabilize the "hypermassive" remnant and may therefore have important dynamical effects (Baumgarte, Shapiro, & Shibata 2000; Lyford, Baumgarte, & Shapiro 2003). However, as we find in this paper, the $m = 1$ mode is unstable only for very soft equations of state, so that it is not obvious that they will arise in the remnant of a binary neutron star merger. However, they may arise in a rapidly spinning proto–neutron star core when surrounded by a fall-back disk, possibly forming a low-mass condensation that can explode and induce a large neutron star recoil speed (Colpi & Wasserman 2002). Finally, the $m = 1$ instability might arise in massive disks around black holes, especially if the disks are radiation dominated and hence governed by a soft equation of state.

This paper is organized as follows. In § 2 we present the basic equations, our initial data, and diagnostics. We discuss our numerical results in § 3 and briefly summarize our findings in § 4. Throughout this paper we use gravitational units[4] with $G = c = 1$ and adopt Cartesian coordinates (x, y, z).

2. BASIC EQUATIONS

2.1. *Newtonian Hydrodynamics*

We construct a $3 + 1$ dimensional Newtonian hydrodynamics code assuming an adiabatic Γ-law equation of state

$$P = (\Gamma - 1)\rho\varepsilon \,, \tag{1}$$

where P is the pressure, Γ the adiabatic index, ρ the mass density, and ε the specific internal energy density. For perfect fluids the Newtonian equations of hydrodynamics then consist of the continuity equation

$$\frac{\partial \rho}{\partial t} + \frac{\partial(\rho v^i)}{\partial x^i} = 0 \,, \tag{2}$$

the energy equation

$$\frac{\partial e}{\partial t} + \frac{\partial(e v^i)}{\partial x^i} = -\frac{1}{\Gamma} e^{-(\Gamma-1)} P_{\rm vis} \frac{\partial v^i}{\partial x^i} \,, \tag{3}$$

and the Euler equation

$$\frac{\partial(\rho v_i)}{\partial t} + \frac{\partial(\rho v_i v^j)}{\partial x^j} = -\frac{\partial(P + P_{\rm vis})}{\partial x^i} - \rho \frac{\partial \Phi}{\partial x^i} \,. \tag{4}$$

Here v^i is the fluid velocity, Φ is the gravitational potential, and e is defined according to

$$e = (\rho\varepsilon)^{1/\Gamma} \,. \tag{5}$$

We compute the artificial viscosity pressure $P_{\rm vis}$ from Richtmyer & Morton (1994)

$$P_{\rm vis} = \begin{cases} C_{\rm vis}\rho(\delta v)^2 & \text{for } \delta v \le 0 \,, \\ 0 & \text{for } \delta v \ge 0 \,, \end{cases} \tag{6}$$

where $\delta v \equiv 2\delta x \partial_i v^i$ and $\delta x (= \Delta x = \Delta y = \Delta z)$ is the local grid spacing, and we choose the dimensionless parameter $C_{\rm vis} = 2$. When evolving the above equations we limit the step size Δt by an appropriately chosen Courant condition.

We have tested the ability of our code to resolve shocks by solving a wall shock problem, in which two phases of a fluid collide at supersonic speeds. In Figure 1 we compare numerical results with the analytic solution for initial velocities that are similar to those found in our simulations below. With $C_{\rm vis} = 2$ we find good agreement for Mach numbers up to $M_{\rm mach} \lesssim 6$. The drop in density at $x = 0$ is usually interpreted as "wall heating" (e.g., Hawley, Smarr, & Wilson 1984).

[4] Since we adopt Newtonian gravity in this paper, the speed of light enters only in the gravitational waveforms (§§ 2.3 and 3).

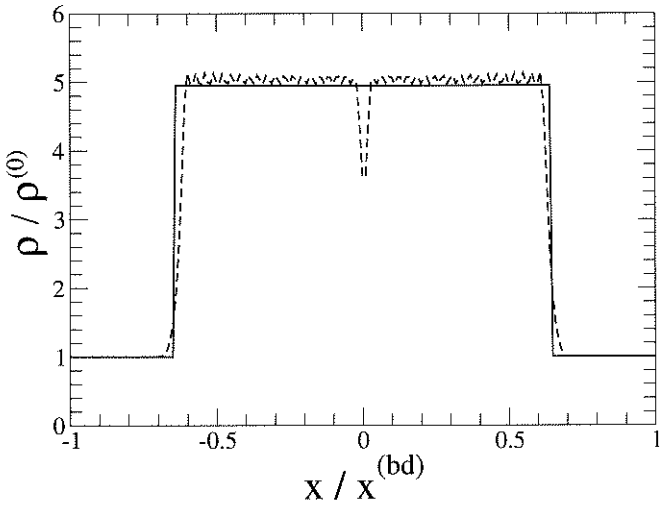

FIG. 1.—Comparison between numerical and analytical results in a one-dimensional wall shock problem at $t = 2.5x^{(\mathrm{bd})}/v_0$ (where the fluid flow is aligned with the x-axis), showing analytic results (*solid lines*) and numerical results (*dashed lines*). For this simulation we chose $\Gamma = 1.30$, $\rho^{(0)} = 2.80 \times 10^{-3}$, $\kappa = 5.85 \times 10^{-2}$, $x^{(\mathrm{bd})} = 0.5$ with a grid space $\delta x = 5 \times 10^{-3}$ and $v_0 = 2.78 v_s$, where v_s is the initial speed of sound.

The gravitational potential is determined by the Poisson equation

$$\triangle\Phi = 4\pi\rho \,, \tag{7}$$

which we solve subject to the outer boundary condition

$$\Phi = -\frac{M}{r} - \frac{d_i x^i}{r^2} + O(r^{-3}) \,. \tag{8}$$

Here M is the total mass

$$M = \int_V \rho \, dx^3 \,, \tag{9}$$

and d_i is the dipole moment

$$d_i = \int_V \rho x_i \, dx^3 \,. \tag{10}$$

2.2. *Initial Data*

As initial data, we construct differentially rotating equilibrium models with an algorithm based on Hachisu (1986). Individual models are parameterized by the ratio of the polar to the equatorial radius R_p/R_{eq} and a parameter of dimension length d that determines the degree of differential rotation through

$$\Omega = \frac{j_0}{d^2 + \varpi^2} \,. \tag{11}$$

Here Ω is the angular velocity, j_0 is a constant parameter with units of specific angular momentum, and ϖ is the cylindrical radius. The parameter d determines the length scale over which Ω changes; uniform rotation is achieved in the limit $d \to \infty$. For the construction of initial data we also assume a polytropic equation of state

$$P = \kappa \rho^{1+1/n} \,, \tag{12}$$

where $n = 1/(\Gamma - 1)$ is the polytropic index and κ a constant. In absence of shocks, the polytropic form of the equation of state is conserved by the Γ-law equation of state (eq. [1]).

To enhance any $m = 1$ or $m = 2$ instability, we disturb the initial equilibrium density ρ_{eq} by a nonaxisymmetric perturbation according to

$$\rho = \rho_{\mathrm{eq}} \left(1 + \delta^{(1)} \frac{x + y}{R_{\mathrm{eq}}} + \delta^{(2)} \frac{x^2 - y^2}{R_{\mathrm{eq}}^2} \right) \,, \tag{13}$$

with $\delta^{(1)} = \delta^{(2)} = 10^{-3}$ in all our simulations.[5]

2.3. *Gravitational Waveforms*

We compute approximate gravitational waveforms by evaluating the quadrupole formula. In the radiation zone, gravitational waves can be described by a transverse traceless perturbed metric h_{ij}^{TT} with respect to a flat spacetime. In the quadrupole formula, h_{ij}^{TT} is found from Misner, Thorne, & Wheeler (1973)

$$h_{ij}^{TT} = \frac{2}{r} \frac{d^2}{dt^2} I_{ij}^{\mathrm{TT}} \,, \tag{14}$$

where r is the distance to the source, I_{ij} is the quadrupole moment of the mass distribution (see eq. [36.42b] in Misner et al. 1973), and TT denotes the transverse traceless projection. Choosing the direction of the wave propagation to be along the z-axis, the two polarization modes of gravitational waves can be determined from

$$h_+ \equiv \tfrac{1}{2}(h_{xx}^{\mathrm{TT}} - h_{yy}^{\mathrm{TT}}) \,, \quad h_\times \equiv h_{xy}^{\mathrm{TT}} \,. \tag{15}$$

For observers along the z-axis, we thus have

$$\frac{r h_+}{M} = \frac{1}{2M} \frac{d}{dt} (\dot{I}_{xx} - \dot{I}_{yy}) \,, \tag{16}$$

$$\frac{r h_\times}{M} = \frac{1}{M} \frac{d}{dt} \dot{I}_{xy} \,. \tag{17}$$

The number of time derivatives I_{ij} that have to be taken can be reduced by using the continuity equation (2)

$$\dot{I}_{ij} = \int (\rho v^i x^j + \rho x^i v^j) d^3x \tag{18}$$

in equations (16) and (17) (see Finn 1989).

2.4. *Numerical Implementation and Diagnostics*

Our code is based on the post-Newtonian hydrodynamics scheme of Shibata, Baumgarte, & Shapiro (1998) and Saijo et al. (2001), to which the reader is referred for a more detailed description, discussion, and tests. We choose the axis of rotation to align with the z-axis and assume planar symmetry across the equator. The equations of hydrodynamics are then solved on a uniform grid of size $169 \times 169 \times 85$. We terminate our simulations either when the central density has increased to a point at which our resolution becomes inadequate or after a sufficient number of central rotation periods (between 20 and 40) for us to detect dynamical instabilities.

[5] The numerical finite difference error is in principle sufficient to trigger instabilities, but starting from such a small amplitude it would take the instability prohibitively long to reach saturation.

We monitor the conservation of mass M (eq. [9]), angular momentum J,

$$J = \int \rho(xv^y - yv^x)d^3x\,, \tag{19}$$

energy E,

$$E = T + U + W = \tfrac{1}{2}\int \rho v^i v_i d^3x + \int \rho\varepsilon d^3x + \tfrac{1}{2}\int \rho\Phi d^3x\,, \tag{20}$$

and the location of the center of mass $x^i_{\rm CM}$

$$x^i_{\rm CM} = \int \rho x^i d^3x\,. \tag{21}$$

Here T is the kinetic energy (all rotational at $t = 0$), U the internal energy, and W the gravitational potential energy. Given our assumption of equatorial symmetry, we have $x^z_{\rm CM} = 0$ identically, so that we need only to monitor the x- and y-components of $x^i_{\rm CM}$. Because of our flux-conserving difference scheme the mass M is also conserved up to round-off error, except if matter leaves the computational grid (which was never more than 0.01% of the total mass). In all cases reported in § 3 the energy E and the angular momentum J were conserved up to ~0.1% of their initial values, and the center of mass moved by less than about 1% of 1 spatial grid cell per central rotation period.

To monitor the development of $m = 1$ and $m = 2$ modes we compute[6] a "dipole diagnostic"

$$D = \langle e^{im\varphi}\rangle_{m=1} = \frac{1}{M}\int \rho\frac{x + iy}{\sqrt{x^2 + y^2}}d^3x \tag{22}$$

and a "quadrupole diagnostic"

$$Q = \langle e^{im\varphi}\rangle_{m=2} = \frac{1}{M}\int \rho\frac{(x^2 - y^2) + i(2xy)}{x^2 + y^2}d^3x\,, \tag{23}$$

where angle brackets denote the density weighted average. In the following we plot only the real parts of D and Q.

3. RESULTS

3.1. *Dynamical Bar Formation*

Before studying $m = 1$ one-armed spiral instabilities, it is useful to test the capability of our code and our diagnostics to detect any instabilities. To do so, we reproduce an $m = 2$ bar mode instability that was recently found by Shibata et al. (2002) in highly differentially rotating $n = 1$ polytropes for surprisingly small values of $T/|W|$. The parameters of our initial data for this test are listed in Table 1. For all our simulations we add a small dipole ($m = 1$) and quadrupole ($m = 2$) perturbation to the initial equilibrium star (eq. [13]) to enhance the growth of any instability.

In Figure 2 we show both diagnostics D and Q as a function of time. The dipole diagnostic D remains very small throughout the evolution (small oscillations are due to the initial perturbation), while the quadrupole diagnostic Q grows exponentially until it saturates. These results indicate

[6] Our diagnostics differ from those in previous treatments (Centrella et al. 2001), in which the growth of the mode is measured at a single arbitrary Eulerian radius in the equatorial plane inside the star.

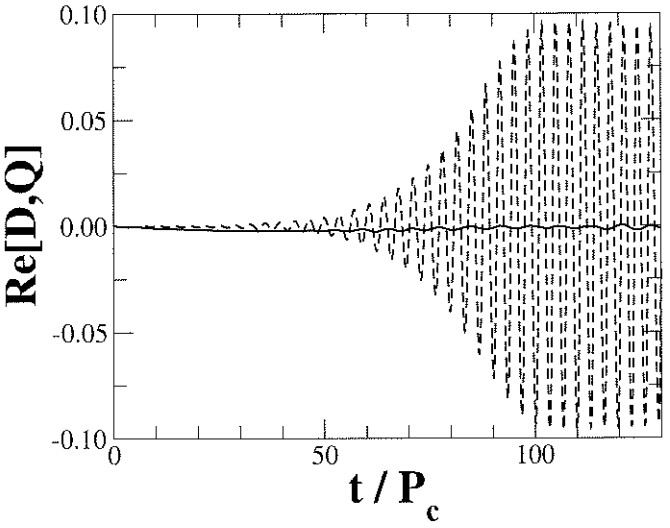

FIG. 2.—Diagnostics D and Q as a function of t/P_c for our bar formation model (see Table 1), showing the values of D (*solid lines*) and Q (*dotted lines*). We terminate our simulation when $t = 132P_c$. Hereafter P_c represents the central rotation period.

that the star is unstable toward bar formation but stable toward one-armed spiral formation. The bar persists without decay for over one surface-rotation period following saturation, corresponding to over 30 central rotation periods. After this we terminate our integration.

The bar mode formation is also evident in Figure 3, which shows a snapshot of the density contours just before we terminate the evolution. Because of the small value of $T/|W|$ the bar is too weak to form double spiral arms. The gravitational waveform emitted by the bar formation is shown in Figure 4. We expect that it will survive without decay until gravitational radiation reaction forces destroy the bar $[\sim(R/M)^{5/2}t_{\rm dyn} \gg t_{\rm dyn}]$.

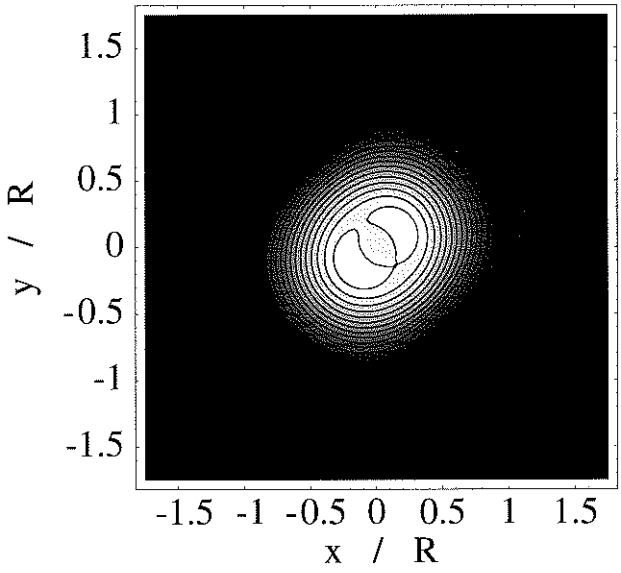

FIG. 3.—Final density contours in the equatorial plane for our bar formation model. Snapshots are plotted at $(t/P_c, \rho_{\rm max}/\rho^{(0)}_{\rm max}) = (132, 1.25)$, where $\rho_{\rm max}$ is the maximum density, $\rho^{(0)}_{\rm max}$ is the initial maximum density, and R is the initial equatorial radius. The contour lines denote densities $\rho/\rho_{\rm max} = 6.67(16 - i) \times 10^{-2}$ $(i = 1, \ldots, 15)$.

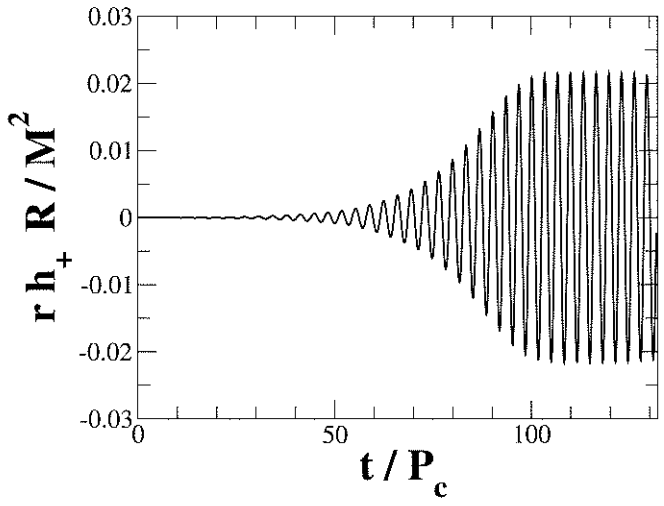

FIG. 4.—Gravitational waveform for a bar-unstable star as seen by a distant observer located on the z-axis.

These simulations indicate that our code and diagnostics are capable of detecting instabilities and also reconfirm the findings of Shibata et al. (2002) that strongly differentially rotating stars can be unstable to dynamical bar mode formation even at very small values of $T/|W|$.

3.2. *Dynamical One-armed Spiral Formation*

We now focus on $m = 1$ one-armed spiral instabilities. Before we analyze their dependence on the stiffness of the equation of state and the degree of differential rotation in the following subsections, we first want to reconfirm the findings of Centrella et al. (2001). To reconstruct their initial data, we adopt a polytropic index of $n = 3.33$ and a high degree of differential rotation ($d/R_e = 0.2$). We study two different models, which are detailed in Table 2. The more rapidly rotating model I (a) (the case $T/|W| = 0.14$ of Centrella et al. 2001) has a toroidal structure, while model I (b) (the case $T/|W| = 0.09$ of Centrella et al. 2001) does not. Confirming the results of Centrella et al. (2001), we find that model I (a) develops an $m = 1$ instability, while model I (b) remains stable.

TABLE 1

INITIAL DATA FOR BAR FORMATION TESTS ($n = 1$)

Parameter	Value
d/R_{eq}[a]	0.20
R_p/R_{eq}[b]	0.250
Ω_c/Ω_{eq}[c]	26.0
ρ_c/ρ_{max}[d]	0.160
R_{maxd}/R_{eq}[e]	0.383
$T/\|W\|$[f]	0.119
$m = 1$	Stable
$m = 2$	Unstable

[a] R_{eq} denotes the equatorial radius.
[b] R_p denotes the polar radius.
[c] Ω_c denotes the central angular velocity, and Ω_{eq} the equatorial angular velocity at the surface.
[d] ρ_c denotes the central density, and ρ_{max} the maximum density.
[e] R_{maxd} denotes the distance between the origin and the location of maximum density.
[f] T denotes the rotational kinetic energy, and W the gravitational potential energy.

TABLE 2

INITIAL DATA FOR THE $m = 1$ TEST ($n = 3.33$)

Parameter	Model I (a)	Model I (b)
d/R_{eq}	0.20	0.20
R_p/R_{eq}	0.417	0.542
Ω_c/Ω_{eq}	26.0	26.0
ρ_c/ρ_{max}	0.531	1.00
R_{maxd}/R_{eq}	0.192	0.00
$T/\|W\|$	0.144	0.090
$m = 1$	Unstable	Stable

The different stability properties of the two models can be seen in Figure 5, where we show both diagnostics D and Q. For model I (b), both diagnostics remain very small, indicating stability,[7] while for model I (a) both diagnostics grow. The dipole diagnostic D, however, grows more strongly than the quadrupole diagnostic Q, indicating that the $m = 1$ mode is the dominant unstable mode. This is also evident in the density contours in Figure 6, which clearly exhibit the one-armed spiral in model I (a) at intermediate times. In all cases that we found to be unstable to an $m = 1$ mode, we simultaneously found a growing $m = 2$ mode.

In Figure 7 we show the maximum density ρ_{max} as a function of time for both models. Even for the stable model I (b) the central density slowly increases over the course of several central rotation periods. This slow growth is due to numerical and artificial viscosity, which tends to decrease the degree of differential rotation. As a consequence, the angular velocity at the center decreases, which also

[7] The small growth of the $m = 1$ mode in model I (b) is a numerical artifact triggered by the initial perturbation; the absence of an exponential growth indicates that this is not an instability.

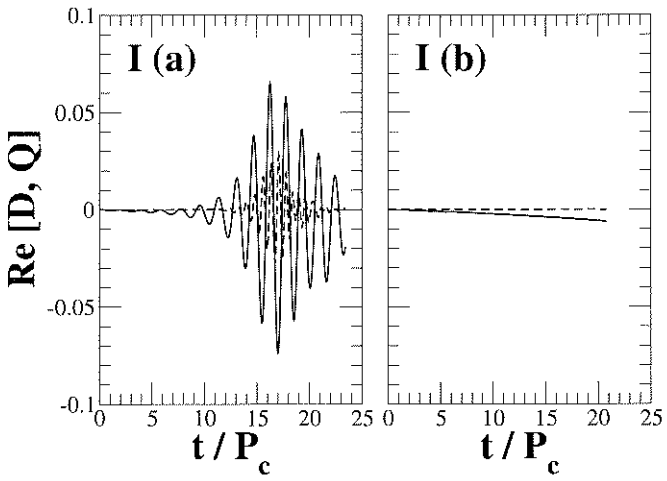

FIG. 5.—Diagnostics D and Q as a function of t/P_c for model I (a) and (b) (see Table 2), showing D (*solid lines*) and Q (*dotted lines*). We terminate our simulation at $t \sim 20P_c$ or when the maximum density of the star exceeds about 10 times its initial value.

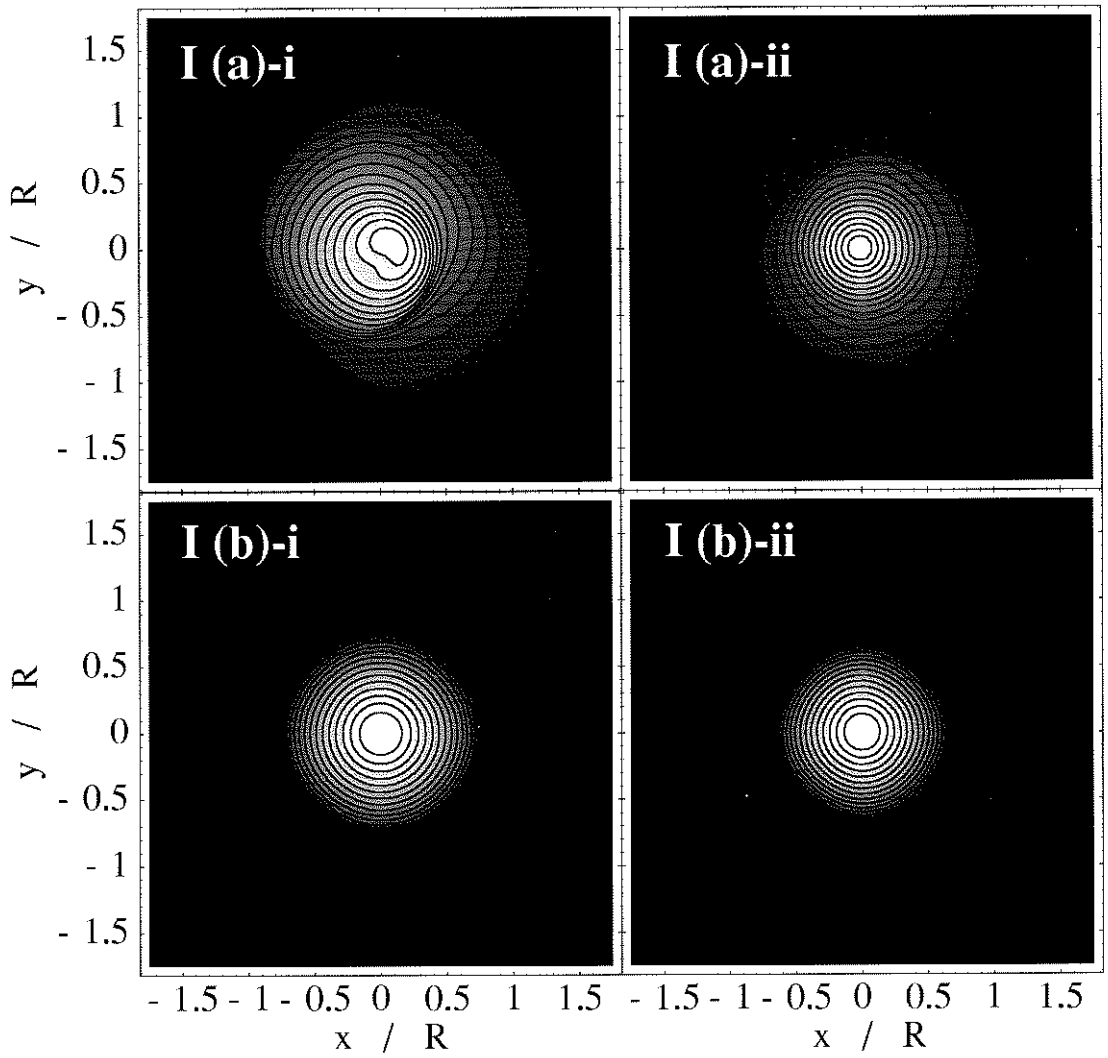

FIG. 6.—Intermediate and final density contours in the equatorial plane for model I (a) and model I (b). Snapshots are plotted at values of $(t/P_c, \rho_{\max}/\rho_{\max}^{(0)}, d)$ equal to (16.3, 3.63, 0.287) for (a)-i, equal to (14.7, 2.08, 0.333) for (b)-i, equal to (23.3, 11.5, 0.287) for (a)-ii, and equal to (20.6, 3.66, 0.333) for (b)-ii. The contour lines denote densities $\rho/\rho_{\max} = 10^{-(16-i)d}$ $(i = 1, \ldots, 15)$.

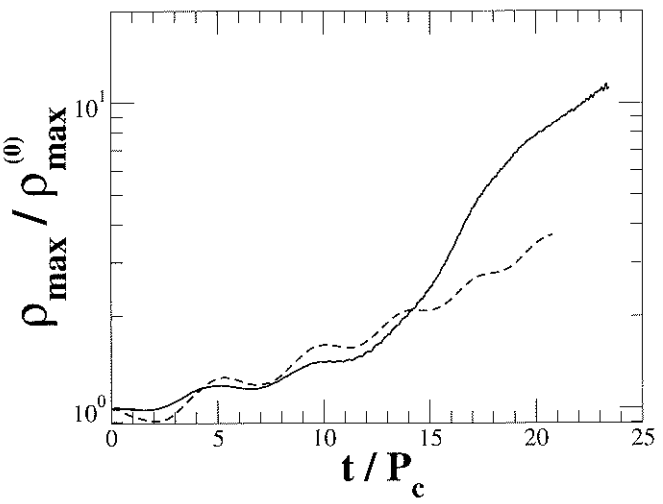

FIG. 7.—Maximum density $\rho_{\max}$ as a function of t/P_c for model I (a) (*solid line*) and model I (b) (*dotted line*). We terminate our simulation at $t \sim 20P_c$ or when the maximum density of the star exceeds about 10 times its initial value, $\rho_{\max}^{(0)}$.

decreases the rotational support of the matter at the center, and hence leads to a slow increase of the central density, even for supposedly stable stars (see also Fig. 8). This effect is a numerical artifact, although viscosities in stars in nature would have a very similar effect. For the unstable model I (b), however, we find a much more rapid increase in the central density. This enhanced increase is caused by the growing spiral instability as it redistributes the matter in the star and destroys the toroidal structure (compare Fig. 8).

Unlike in bar formation, in which the bar persists for many rotational periods (compare § 3.1; Brown 2000; Saijo et al. 2001), we find that D and Q start decreasing immediately after reaching a maximum (see Fig. 5; note that the decrease in D is not as dramatic as the decrease in Q). This is also evident in Figure 6, in which the density contours approach axisymmetry at late times. As the spiral arm propagates through the star, it rearranges the density profile, eliminates the toroidal structure, and ultimately leads to a new axisymmetric equilibrium configuration.

In Figure 9 we show the gravitational wave signal emitted from this instability. Gravitational radiation couples to quadrupole moments, and the emitted radiation therefore

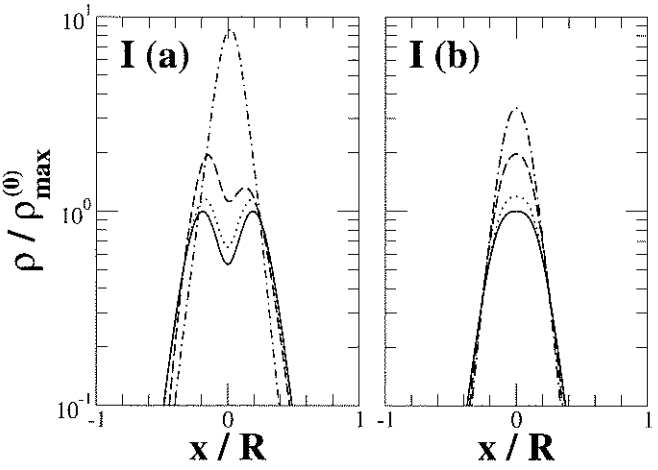

FIG. 8.—Density profiles along the x-axis during the evolution for models I (a) and I (b). Solid, dotted, dashed, and dash-dotted lines, respectively, denote times $t/P_c = 1.16 \times 10^{-3}$, 6.99, 14.0, and 21.0 for I (a) and 7.36×10^{-4}, 6.63, 13.3, and 19.9 for I (b). Note that the density distribution develops asymmetrically in the presence of the $m = 1$ mode instability and that this instability destroys the toroidal structure.

scales with the quadrupole diagnostic Q, which we always find excited along with the $m = 1$ instability. We consistently find that the pattern period of the $m = 2$ modes is very similar to that of the $m = 1$ mode, suggesting that the former is a harmonic of the latter (see Table 3). Since the diagnostic Q does not remain at its maximum amplitude after saturating, we find that the gravitational wave amplitude is not nearly as persistent as for the bar mode instability. We also find that the gravitational wave period, here $P_{GW} \sim 0.7P_c \sim \Omega_c^{-1}$, is different from the value $P_{GW} \sim 3.3P_c \sim \Omega_{eq}^{-1}$ we found for the bar mode in § 3.1, which points to a difference in the generation mechanism. Characteristic wave frequencies f_{GW} correspond to the central rotation period of the star.

The results of this subsection confirm the findings of Centrella et al. (2001) and establish that stars with soft equations of state and large degrees of differential rotation are unstable to one-armed spiral arm formation. Such stars

TABLE 3

COMPARISON OF PATTERN PERIODS

Model	Period of $m = 1$ Mode (P_c)	Period of $m = 2$ Mode (P_c)	Pattern Period (P_c)
I (a)[a]	1.6	0.7	1.4
II (b)[b]	2.5	1.2	2.4
II (c)[b]	2.0	1.0	2.0
II (d)[b]	1.6	0.7	1.4
III (c)[c]	1.6	0.7	1.4
III (d)[c]	1.6	0.7	1.4

[a] See Fig. 5.
[b] See Fig. 10.
[c] See Fig. 15.

have a toroidal structure, which is erased by the growing $m = 1$ mode. One might be led to believe that this toroidal structure is a necessary and perhaps even a sufficient condition for the growth of the $m = 1$ instability. In the following two subsections we analyze the dependence of the onset of instability on both the stiffness of the equation of state and the degree of differential rotation and find that toroidal structure alone is not sufficient for a one-armed spiral instability.

3.3. *Stiffness of the Equation of State*

We parameterize the stiffness of the equation of state by varying the polytropic index n between $n = 3.33$ and $n = 2$. In this sequence we keep the degree of differential rotation (i.e., d and hence Ω_c/Ω_{eq}) fixed and adjust the overall rotation rate (parameterized by R_p/R_{eq}) so that the value of $T/|W|$ remains very close to 0.144 (as for model I [a]). We list our four different models II in Table 4 and note that model II (d) is identical to model I (a).

Figure 10, where we plot the dipole diagnostic D as a function of time, clearly shows that an $m = 1$ instability is excited in models II (b) and II (c) in addition to model II (d). After reaching saturation, D decreases again, similar to model I (a), which we described in detail in § 3.2. Model II (a), however, which has the most pronounced toroidal

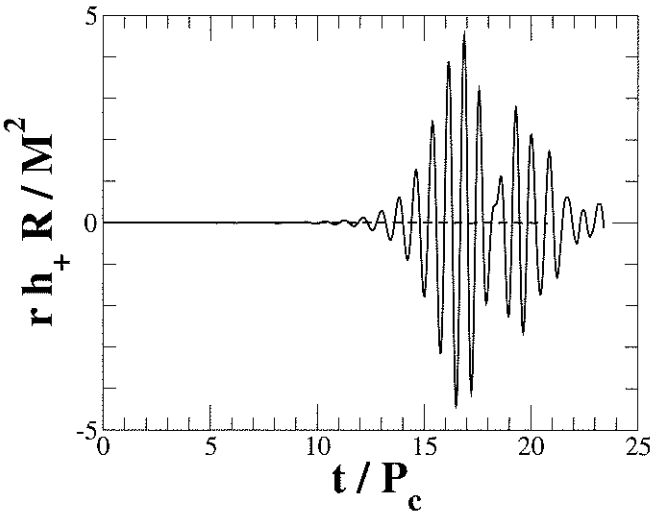

FIG. 9.—Gravitational waveforms as seen by a distant observer located on the z-axis for model I (a) (*solid line*) and model I (b) (*dashed line*).

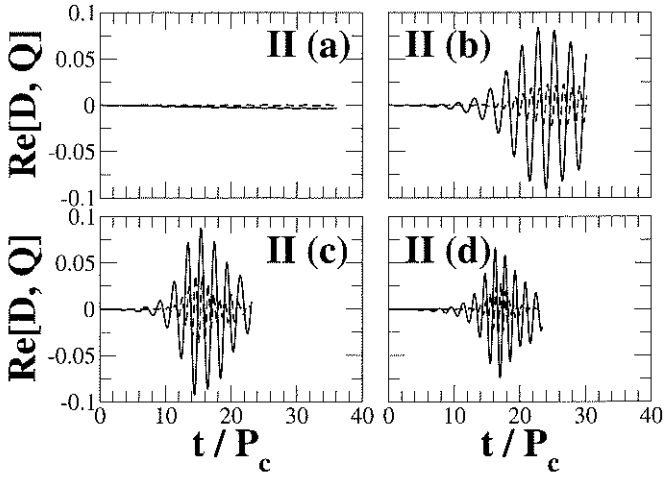

FIG. 10.—Diagnostics D and Q as a function of t/P_c for models II (see Table 4). Solid and dotted lines denote D and Q. We terminate our simulation at $t \sim 25P_c$ or when the maximum density of the star exceeds about 10 times its initial value.

TABLE 4

INITIAL DATA SEQUENCE VARYING THE POLYTROPIC INDEX

Model	n[a]	d/R_{eq}	R_p/R_{eq}	Ω_c/Ω_{eq}	ρ_c/ρ_{max}	R_{maxd}/R_{eq}	$T/\|W\|$	$m = 1$ Stability
II (a)	2.00	0.20	0.271	26.0	0.091	0.349	0.145	Stable
II (b)	2.50	0.20	0.354	26.0	0.193	0.295	0.145	Unstable
II (c)	3.00	0.20	0.396	26.0	0.325	0.243	0.147	Unstable
II (d)[b]	3.33	0.20	0.417	26.0	0.531	0.192	0.144	Unstable

[a] Polytropic index.
[b] Same as model I (a).

structure, remains stable. These findings are also evident in Figure 11, where we show density contours of intermediate and final configurations.

In Figure 12, we show the maximum density as a function of time. As we have seen in § 3.2, the maximum density slowly increases in all cases because of dissipation of differential rotation. Once the one-armed spiral forms in models II (b) and II (c), however, this increase is much more rapid, which indicates again that the unstable mode rearranges the matter in the star and destroys the toroidal structure. This effect can also be seen in the density profiles in Figure 13.

We show the gravitational wave signal emitted from models II in Figure 14. As we found in § 3.2, consistent with the diagnostics D and Q, the gravitational wave signal emitted by the one-armed spiral mode does not persist over many rotational periods and instead decays fairly rapidly after it has been excited. This characteristic is very different from what has been found for $m = 2$ bar mode instabilities (compare § 3.1 and Brown 2000; Saijo et al. 2001). We also find that the maximum wave amplitude is much smaller than can be found for configurations unstable to a pure bar mode (compare Fig. 4) as gravitational radiation requires a quadrupole distortion and the $m = 2$ perturbation in models II is being excited only as a lower amplitude harmonic of the $m = 1$ mode (as suggested by a comparison of the pattern periods; see Table 3).

3.4. *Degree of Differential Rotation*

We now focus on the dependence of the one-armed spiral instability on the degree of differential rotation. Starting again with model I (a), we now increase the parameter d to explore more modest degrees of differential rotations. As before, we would like to keep $\beta \sim 0.14$ in this sequence. For very soft equations of state, this value can be achieved only for very strong degrees of differential rotation. Therefore, to keep β approximately constant, we simultaneously have to decrease n as we decrease the degree of differential rotation.[8] We list the details of our models III in Table 5.

We show the dipole diagnostic D as a function of time in Figure 15, which shows that models III (a) and III (b) are stable against one-armed spiral formation while models III (c) and III (d) (which is the same as model I [a]) are not. The same conclusion can be drawn from the density snapshots in Figure 16. As in § 3.3, we find that the one-armed spiral results in a large increase in the central density (Fig. 17) and an elimination of the toroidal structure (Fig. 18). Tohline & Hachisu (1990) similarly found that the elimination of the toroidal structure is related to an outward transport of angular momentum. To quantify this effect, we monitored the angular momentum distribution in model III (d) by computing a mean radius of angular momentum

$$\langle j \rangle = \frac{M\left[\int dv\rho\sqrt{x^2+y^2}(xv^y - yv^x)\right]}{J\left(\int dv\rho\sqrt{x^2+y^2}\right)} . \qquad (24)$$

This mean radius is initially 1.1 but increases to 1.5 at $t = 24.5P_c$, indicating that in fact the $m = 1$ mode transports angular momentum outward.

We show gravitational waveforms from models III in Figure 19. We again find that the amplitude decreases after reaching a maximum, which is a typical behavior of $m = 1$ instability (in Table 3 the pattern period of diagnostics D and Q is the same). In some cases, however, this decrease is not monotonic, and the amplitude may increase again to form several distinct wave packets. Our numerical data are not sufficient to determine the generic character of the gravitational waves emitted from $m = 1$ instabilities, and we expect that this will be subject of future investigations. The problem is that the growth of central concentration during the evolution exceeds the ability of our code to resolve the innermost regions for arbitrary long times in all cases.

[8] This means that our results do not separate the dependence on the degree of differential rotation from the dependence on the stiffness of the equation of state as cleanly as one might wish.

TABLE 5

INITIAL DATA SEQUENCE VARYING THE DEGREE OF DIFFERENTIAL ROTATION

Model	n	d/R_{eq}	R_p/R_{eq}	Ω_c/Ω_{eq}	ρ_c/ρ_{max}	R_{maxd}/R_{eq}	$T/\|W\|$	$m = 1$ Stability
III (a)	1.00	0.62	0.500	3.60	0.992	0.189	0.150	Stable
III (b)	2.00	0.41	0.479	6.95	0.935	0.198	0.150	Stable
III (c)	3.00	0.25	0.438	17.0	0.695	0.197	0.147	Unstable
III (d)[a]	3.33	0.20	0.417	26.0	0.531	0.192	0.144	Unstable

[a] Model I (a) in Table. 2.

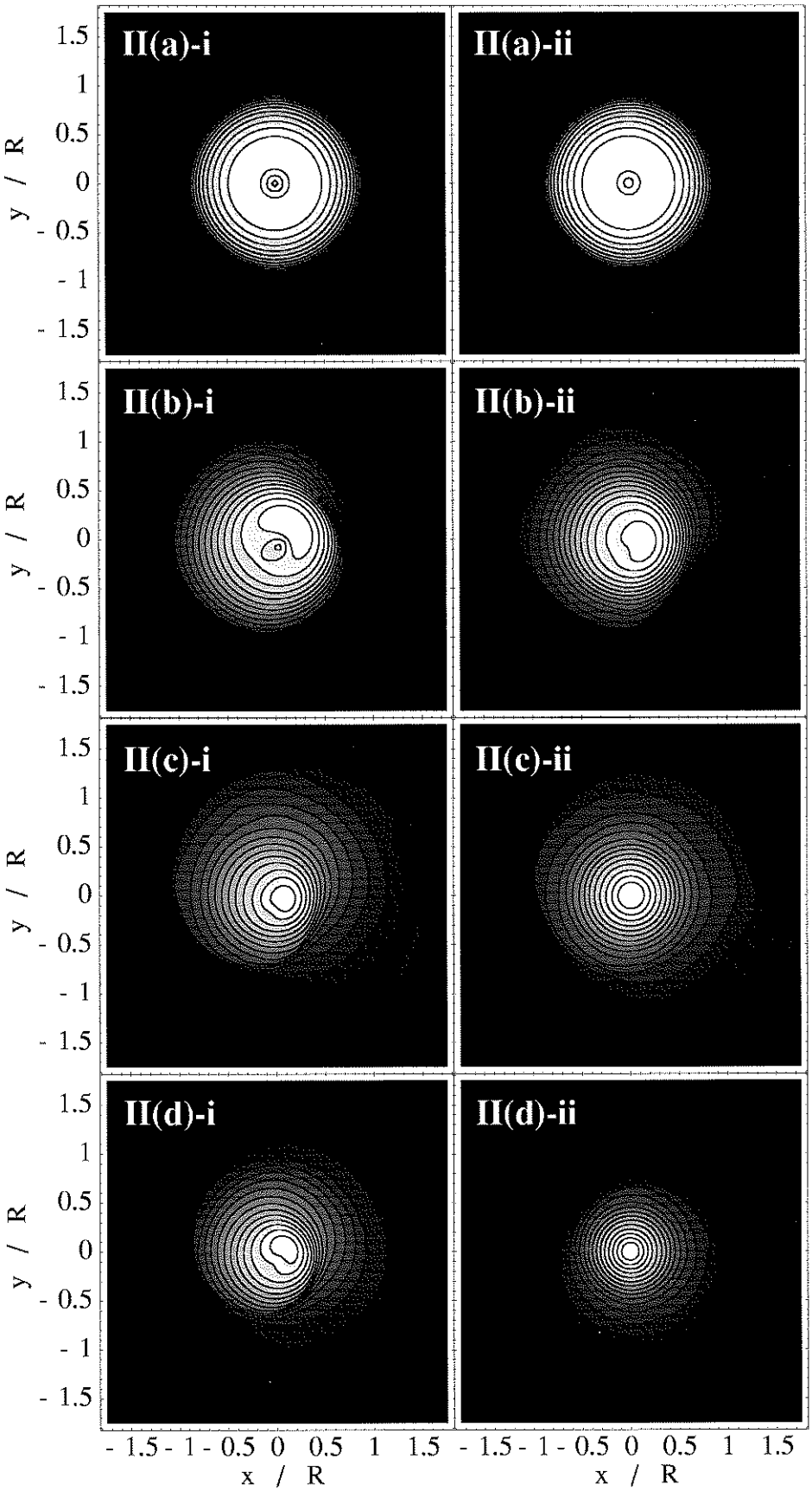

FIG. 11.—Intermediate and final density contours in the equatorial plane for models II. Snapshots are plotted at values of $(t/P_c, \rho_{\max}/\rho_{\max}^{(0)}, d)$ equal to (23.8, 1.14, 0.220), for II (a)-i, equal to (20.6, 1.90, 0.220) for II (b)-i, equal to (17.3, 4.98, 0.287) for II (c)-i, equal to (16.3, 3.63, 0.287) for II (d)-i, equal to (34.7, 1.24, 0.220) for II (a)-ii, equal to (30.1, 2.92, 0.220) for II (b)-ii, equal to (25.2, 7.41, 0.287) for II (c)-ii, and equal to (23.3, 11.5, 0.287) for II (d)-ii. The contour lines denote densities $\rho/\rho_{\max} = 10^{-(16-i)d}$ $(i = 1, \ldots, 15)$.

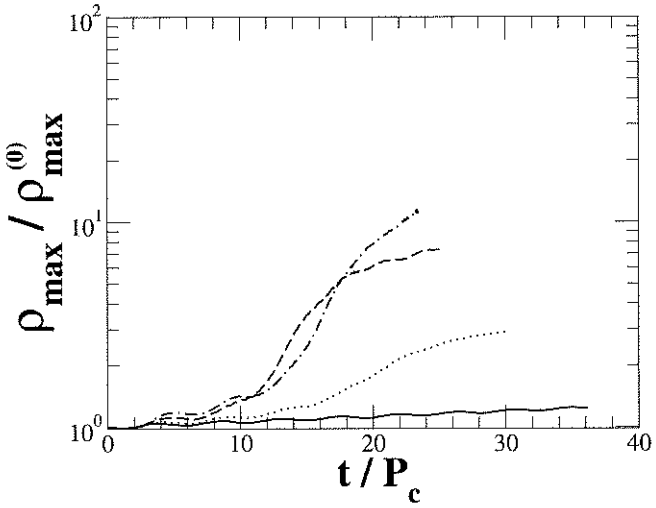

FIG. 12.—Maximum density ρ_{max} as a function of t/P_c for model II (a) (*solid line*), model II (b) (*dotted line*), model II (c) (*dashed line*), and model II (d) (*dash-dotted line*).

4. DISCUSSION

We have studied the conditions under which Newtonian differentially rotating stars are dynamically unstable to an $m = 1$ one-armed spiral instability and found that both soft equations of state and a high degree of differential rotation are necessary to trigger the instability. For sufficiently soft equations of state and sufficiently high degrees of differential rotation we found that stars are dynamically unstable even at the small values of $T/|W| \sim 0.14$ considered in this paper.

While we find that a toroidal structure alone is not sufficient for the $m = 1$ instability, all the models that are unstable do have a toroidal structure, suggesting that this may be a necessary condition. The growing $m = 1$ mode redistributes both matter and angular momentum in the unstable star and destroys the toroidal structure after a few central rotation periods.

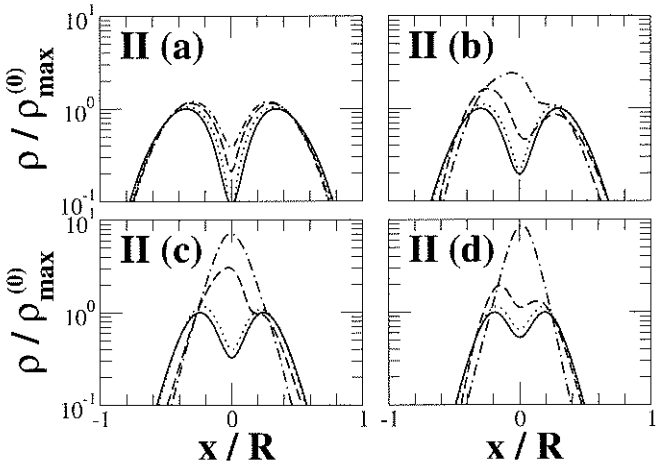

FIG. 13.—Density profiles along the x-axis during the evolution of models II. Solid, dotted, dashed, dash-dotted line, respectively, denote times $t/P_c = 2.17 \times 10^{-3}$, 10.8, 21.7, and 32.5 for II (a), 1.56×10^{-3}, 9.56, 19.0, and 28.5 for II (b), 1.33×10^{-3}, 7.97, 15.9, and 23.9 for II (c), and 1.16×10^{-3}, 6.98, 14.0, and 21.0 for II (d). Note that the toroidal structure vanishes at late times for models II (b), II (c), and II (d).

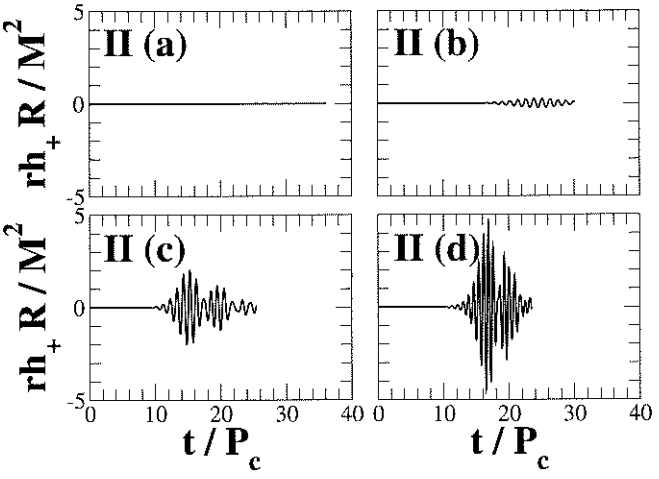

FIG. 14.—Gravitational waveforms as seen by a distant observer located on the z-axis for models II.

Quasi-periodic gravitational waves emitted by stars with $m = 1$ instabilities have smaller amplitudes than those emitted by stars unstable to the $m = 2$ bar mode. For $m = 1$ modes, the gravitational radiation is emitted not by the primary mode itself, but by the $m = 2$ secondary harmonic, which is simultaneously excited, albeit at a lower amplitude (see Fig. 5). Unlike the case for bar-unstable stars, the gravitational wave signal does not persist for many periods but instead is damped fairly rapidly in most of the cases we have examined.

We have plotted typical wave forms for stars unstable to $m = 2$ bar modes in Figure 4 and for stars unstable to one-armed spiral $m = 1$ modes in Figures 9, 14, and 19. Characteristic wave frequencies f_{GW} are seen to be $\sim P_c^{-1} \sim \Omega_c$ and are considerably higher than $\Omega_{eq} \lesssim (M/R^3)^{1/2}$ because of appreciable differential rotation. For supermassive stars ($M \gtrsim 10^5\ M_\odot$) the amplitudes and frequencies of these waves fall well within the detectable range of the Laser Interferometer Space Antenna (see, e.g., New & Shapiro 2001).

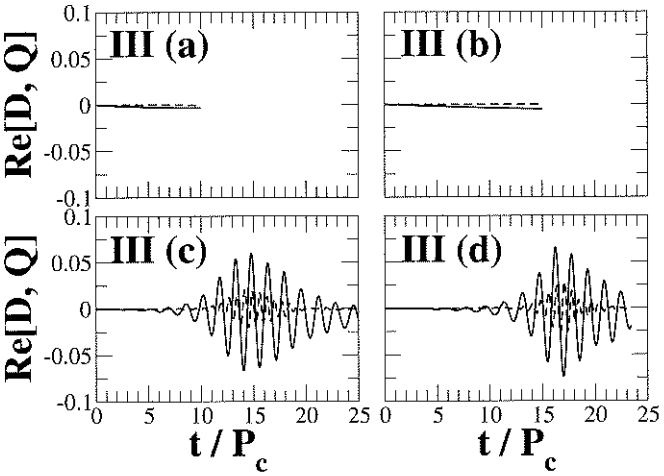

FIG. 15.—Diagnostics D and Q as a function of t/P_c for models III (see Table 5), showing D (*solid line*) and Q (*dotted line*).

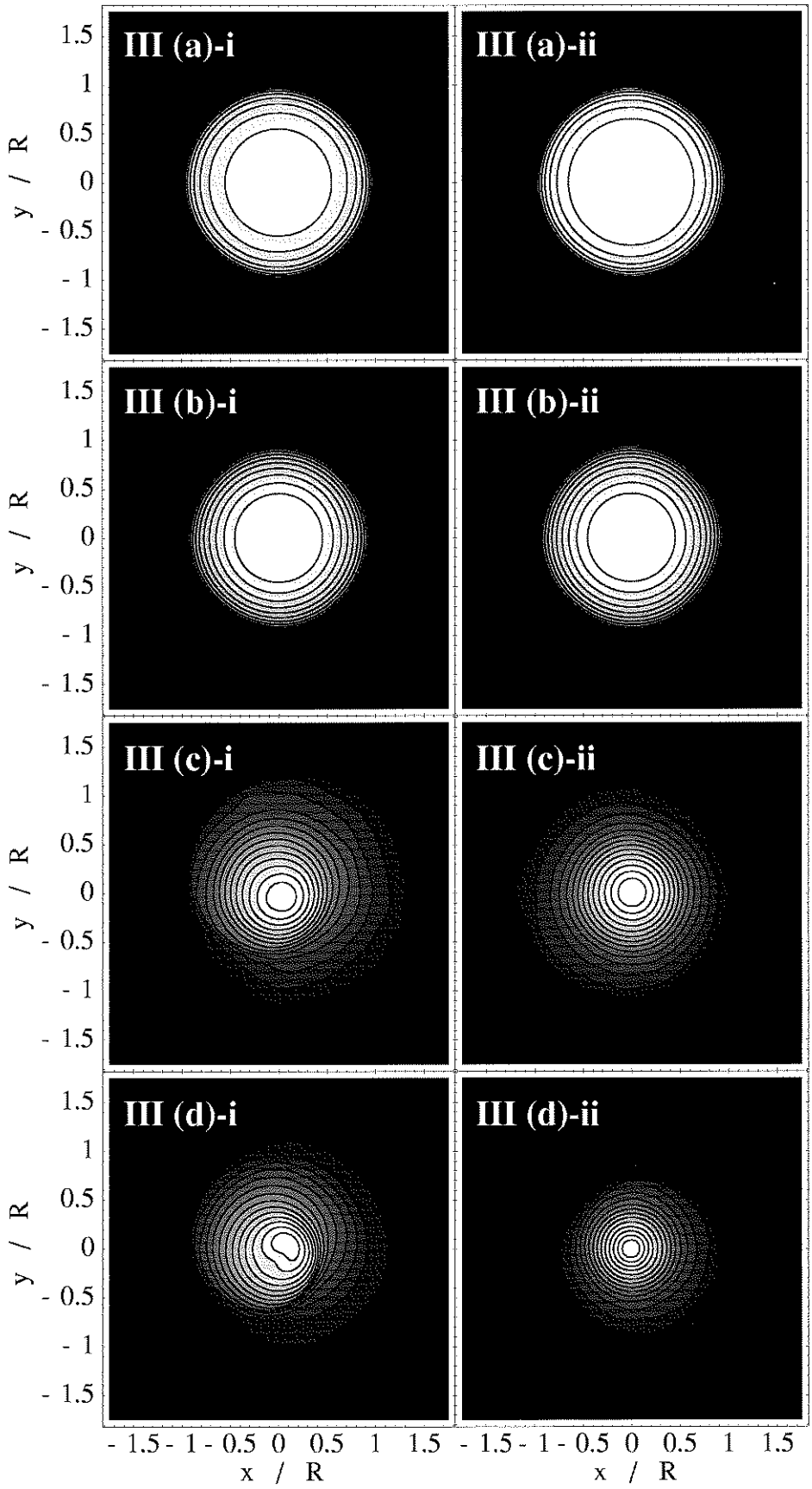

FIG. 16.—Intermediate and final density contours in the equatorial plane for models III. Snapshots are plotted at values of $(t/P_c, \rho_{\max}/\rho_{\max}^{(0)}, d)$ equal to (6.81, 1.01, 0.200) for for III (a)-i, equal to (10.4, 1.07, 0.267) for III (b)-i, equal to (17.6, 3.72, 0.287) for III (c)-i, equal to (16.3, 3.63, 0.287) for III (d)-i, equal to (9.90, 1.02, 0.200) for III (a)-ii, equal to (14.8, 1.09, 0.267) for III (b)-ii, equal to (25.6, 5.05, 0.287), for III (c)-ii, and equal to (23.3, 11.5, 0.287) for III (d)-ii. The contour lines denote densities $\rho = \rho_{\max} \times 10^{-(16-i)d}$ $(i = 1, \ldots, 15)$.

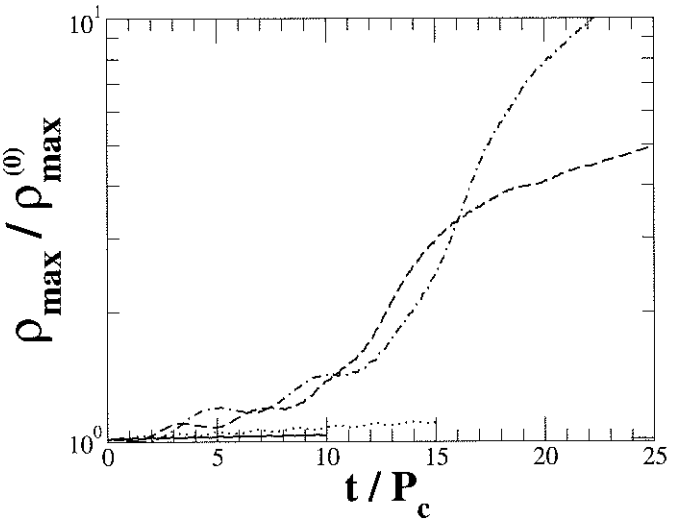

FIG. 17.—Maximum density ρ_{max} as a function of t/P_c for model III (a) (*solid line*), model III (b) (*dotted line*), model III (c) (*dashed line*), and model III (d) (*dash-dotted line*).

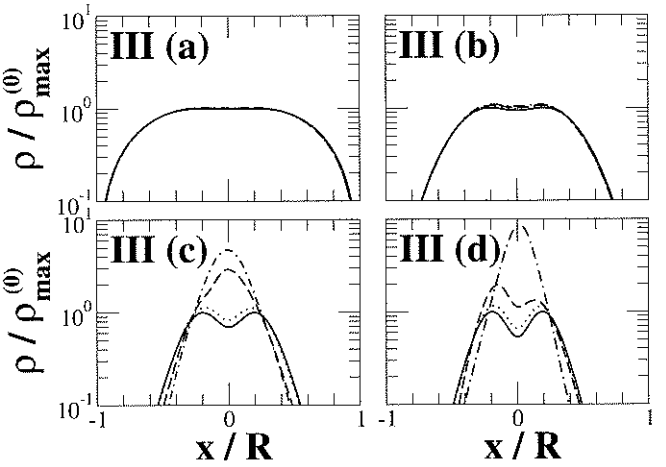

FIG. 18.—Density profiles along the x-axis during the evolution for models III. Solid, dotted, dashed, and dash-dotted lines, respectively, denote times $t/P_c = 3.09 \times 10^{-4}$, 3.09, 6.19, 9.28 for III (a), 4.95×10^{-4}, 4.95, 9.89, 14.8 for III (b), 8.82×10^{-4}, 8.82, 17.6, 26.4 for III (c), and 1.16×10^{-3}, 6.99, 14.0, 21.0 for III (d). Note that the toroidal structure vanishes at the late time in models III (*c*) and III (*d*).

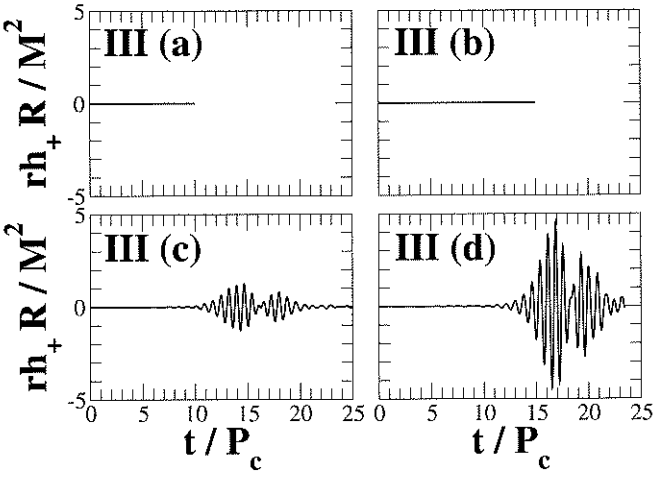

FIG. 19.—Gravitational waveforms as seen by a distant observer located on the z-axis for models III.

We thank an anonymous referee for the careful reading of this manuscript and many constructive suggestions. This work was supported by a JSPS Grant-in-Aid for young scientists (No. 1400927), NSF grants PHY-0090310 and PHY-0205155, and NASA grant NAG 5-10781 at the University of Illinois at Urbana-Champaign and NSF grant PHY-0139907 at Bowdoin College. Numerical computations were performed on the NEC SX-5 machine in the Yukawa Institute for Theoretical Physics, Kyoto University, on the VPP-800 machine in the Academic Center for Computing and Media Studies, Kyoto University, and on the VPP-5000 machine in the Astronomical Data Analysis Center, National Astronomical Observatory of Japan. M. S. thanks Department of Physics, University of Illinois at Urbana-Champaign for their hospitality.

REFERENCES

Adams, F. C., Ruden, S. P., & Shu, F. H. 1989, ApJ, 347, 959
Baumgarte, T. W., Shapiro, S. L., & Shibata, M. 2000, ApJ, 528, L29
Bonnell, I. A. 1994, MNRAS, 269, 837
Brown, J. D. 2000, Phys. Rev. D, 62, 084024
Centrella, J. M., New, K. C. B., Lowe, L. L., & Brown, J. D. 2001, ApJ, 550, L193
Chandrasekhar, S. 1969, Ellipsoidal Figures of Equilibrium (New York: Yale Univ. Press), 61
Colpi, M., & Wasserman, I. 2002, ApJ, 581, 1271
Durisen, R. H., Gingold, R. A., Tohline, J. E., & Boss, A. P. 1986, ApJ, 305, 281
Finn, L. S. 1989, in Frontiers in Numerical Relativity, ed. C. R. Evans, L. S. Finn, & D. W. Hobill (Cambridge: Cambridge Univ. Press), 126
Hachisu, I. 1986, ApJS, 61, 479
Hawley, J. F., Smarr, L. L., & Wilson, J. R. 1984, ApJS, 55, 211
Heemskerk, M. H. M., Papaloizou, J. C., & Savonije, G. J. 1992, A&A, 260, 161
Houser, J. L., & Centrella, J. M. 1996, Phys. Rev. D, 54, 7278
Houser, J. L., Centrella, J. M., & Smith, S. C. 1994, Phys. Rev. Lett., 72, 1314
Laughlin, G., & Bodenheimer, P. 1994, ApJ, 436, 335
Lyford, N., Baumgarte, T. W., & Shapiro, S. L. 2003, ApJ, 583, 410
Misner, C. W., Thorne, K. S., & Wheeler, J. A. 1973, Gravitation (New York: Freeman)
New, K. C. B., Centrella, J. M., & Tohline, J. E. 2000, Phys. Rev. D, 62, 064019
New, K. C. B., & Shapiro, S. L. 2001, ApJ, 548, 439
Pickett, B. K., Durisen, R. H., & Davis, G. A. 1996, ApJ, 458, 714
Richtmyer, R. D., & Morton, K. W. 1994, Difference Metheods for Initial Value Problems (Malabar: Krieger), 313

Saijo, M., Shibata, M., Baumgarte, T. W., & Shapiro, S. L. 2001, ApJ, 548, 919
Shibata, M., Baumgarte, T. W., & Shapiro, S. L. 1998, Phys. Rev. D, 58, 23002
———. 2000, ApJ, 542, 453
Shibata, M., Karino, S., & Eriguchi, Y. 2002, MNRAS, 334, L27
———. 2003, MNRAS, 343, 619
Shibata, M., & Uryū, K. 2000, Phys. Rev. D, 61, 064001
———. 2002, Prog. Theor. Phys., 107, 265
Shu, F. H., Tremaine, S., Adams, F. C., & Ruden, S. P. 1990, ApJ, 358, 495
Smith, S. C., Houser, J. L., & Centrella, J. M. 1996, ApJ, 458, 236
Tassoul, J. 1978, Theory of Rotating Stars (Princeton: Princeton Univ. Press)
Tohline, J. E., Durisen, R. H., & McCollough, M. 1985, ApJ, 298, 220
Tohline, J. E., & Hachisu, I. 1990, ApJ, 361, 394
Toman, J., Imamura, J. N., Pickett, B. J., & Durisen, R. H. 1998, ApJ, 497, 370
Williams, H. A., & Tohline, J. E. 1988, ApJ, 334, 449
Woodward, J. W., Tohline, J. E., & Hachisu, I. 1994, ApJ, 420, 247